Three-dimensional integral equation approach to light scattering, extinction cross sections, local density of states, and quasi-normal modes

Jakob Rosenkrantz de Lasson,* Jesper Mørk, and Philip Trøst Kristensen

DTU Fotonik, Department of Photonics Engineering, Technical University of Denmark, Ørsteds Plads, Building 343, Kongens Lyngby DK-2800, Denmark
Corresponding author: jakob@jakobrdl.dk

We present a numerical formalism for solving the Lippmann–Schwinger equation for the electric field in three dimensions. The formalism may be applied to scatterers of different shapes and embedded in different background media, and we develop it in detail for the specific case of spherical scatterers in a homogeneous background medium. In addition, we show how several physically important quantities may readily be calculated with the formalism. These quantities include the extinction cross section, the total Green's tensor, the projected local density of states, and the Purcell factor as well as the quasi-normal modes of leaky resonators with the associated resonance frequencies and quality factors. We demonstrate the calculations for the well-known plasmonic dimer consisting of two silver nanoparticles and thus illustrate the versatility of the formalism for use in modeling of advanced nanophotonic devices.   © 2013 Optical Society of America

1. INTRODUCTION

Realization of optical devices based on optical micro or nanostructures such as photonic crystals [1–3] or plasmonic nanoparticles [4–6] rely on a prolific interplay between advanced fabrication techniques and accurate numerical methods. The latter paves the way for the design of advanced optical functionalities as well as systematic studies and in-depth understanding of the physical mechanisms at play. Additionally, numerical modeling serves as an indispensable tool in the interpretation of experimental results, and the study and development of numerical modeling methods therefore remain an important and integral part of modern nanophotonics research. Propagation of light, in the form of electromagnetic fields, is governed by Maxwell's equations, and in spite of being known for more than a century, these equations remain very difficult to solve and display rich behavior. Analytical solutions are available only for a limited number of geometries, and numerical solvers are thus indispensable in the design of practical devices. Each numerical scheme has advantages and limitations, as analyzed, for example, with photonic-crystal-based vertical-cavity surface-emitting lasers as benchmark structures using four different methods in [7]. The most prominent advantages of the integral equation approach that we present in this paper are versatility in the form of easy access to figures of merit and high accuracy with a built-in error measure.

The most popular numerical methods in the field of nanophotonics are the finite-difference time-domain (FDTD) method [8] and the finite element method (FEM) [9], which are both based on spatial discretization of Maxwell's equations. FDTD uses a rectangular grid and a simple time-stepping procedure to evolve the fields in time, whereas FEM uses a non-uniform triangular meshing, which can more easily adapt to curved surfaces, and is most often used for frequency-domain problems. As a powerful hybrid approach, discontinuous Galerkin methods use a variant of FEM based on nonoverlapping basis functions, leading to improved performance in time-domain calculations [10]. These methods can easily be adapted to treat arbitrary structures, but the necessity to discretize the entire space may in practice lead to large requirements in terms of memory and computational power, in particular for three-dimensional (3D) problems. Alternatives include modal expansion techniques such as the Fourier modal method [11] and the Rayleigh multipole method [12], in which the fields are expanded on a chosen set of basis functions, and the electromagnetic boundary conditions (BCs) are satisfied to determine the expansion coefficients. In FDTD, FEM, and modal expansion techniques the need to minimize parasitic reflections from the calculation domain boundaries usually entails the introduction of perfectly matched layers (PMLs) [13]. Another class of methods is based on surface or volume integrals [14]. One advantage of this procedure is that only bounded parts of space need to be discretized, which prompts faster computations. Typical approaches employ expansions of the fields on orthonormal sets of basis functions, and the integral equations are converted into systems of linear equations for the expansion coefficients. A popular choice of basis functions is the so-called pulse basis functions [15] that form the foundation of the discrete dipole approximation [16]. The simplicity of these piecewise-constant basis functions allows a simple treatment of arbitrary geometries, but their simplicity in turn leads to very large systems of equations. More severely, the pulse basis functions

induce fictitious current densities, which lead to inaccurate results for high-index contrasts [15].

In this work, we present a volume integral formulation based on the Lippmann–Schwinger equation [17] and the electromagnetic Green's tensor for the electric field. In this approach, the electric field satisfies the radiation condition [18] by construction, and artificial BCs like PMLs are not needed. Known results for the Green's tensor may be used to model inhomogeneities embedded in different background environments such as homogeneous space or layered media [14,19,20]. As an alternative to the pulse basis functions, we employ expansions in scalar wavefunctions that are solutions of a homogeneous Helmholtz equation [21]. The method was developed for 2D structures in [22]; in this work we generalize the method to 3D structures and elaborate on the versatility of the method for calculating various physically important quantities. The general procedure can be applied to scatterers of different shapes in different background environments, but we focus here on the specific example of spherical particles embedded in a homogeneous background medium. In this case the calculation of the ensuing matrix elements dramatically simplifies and can be expressed analytically. The special case of scattering by a single particle is described by Mie scattering theory [23], and generalized Mie theories for several spherical particles have been developed [24–26]. Common ingredients in these schemes are expansions in scalar (or spherical) wavefunctions as well as the use of addition and translation theorems. These functions and theorems are also employed in the present formalism, but whereas the generalized Mie theories rely on explicit fulfillment of the electromagnetic BCs to determine expansion coefficients, our approach exploits the Lippmann–Schwinger equation that implicitly satisfies the BCs. The present formalism is advantageous as it gives direct access to a large number of physically relevant quantities, such as the electric field, including the near- and far-fields [14]; the extinction, scattering, and absorption cross sections [27]; the total Green's tensor for background medium plus scatterers [19,28]; the projected local density of states (LDOS) [14,29]; and the Purcell factor [30] as well as quasi-normal modes (or cavity modes) with their associated Q factors [14,31,32]. Additionally, the formalism contains an explicit error estimate that we demonstrate and discuss. As an application of the formalism, we consider a plasmonic dimer. This system has been widely studied, both experimentally and theoretically, and we choose this well-known material configuration to display how the different physically important quantities can be directly analyzed with the method. Calculation examples using up to 20 particles are demonstrated in [33].

The article is organized as follows: Section 2 presents the details of the formalism, including the introduction of the Lippmann–Schwinger equation, the expansion of the electric field, and the evaluation of the matrix elements. It is shown how the extinction efficiency, the Green's tensor, and the projected LDOS are obtained within our framework. Section 3 provides example calculations for a plasmonic dimer. Specifically, plane wave scattering on the dimer is demonstrated via the excitation of localized surface plasmons (LSPs) in the vicinity of the dimer, and extinction efficiency spectra are presented and discussed. Furthermore, calculations of the Green's tensor and the Purcell factor for the dimer are

performed, and two different modes of the dimer are determined and visualized. Finally, Section 4 concludes the work. A number of appendices give various definitions and detailed expressions, and it is our hope that the interested reader will be able to implement and apply the formalism with a relatively small effort.

2. MULTIPLE-SCATTERING FORMALISM

A. Lippmann–Schwinger Equation

We consider scattering of an incoming electric field, $\mathbf{E}_B$, on N spherical scattering objects embedded in a homogeneous space of relative permittivity $\epsilon_B(\omega)$. The scattering objects have relative permittivities $\epsilon_j(\omega)$, $j = 1, 2, \ldots, N$, and we assume nonmagnetic, isotropic scatterers throughout. Figure 1 shows an example with $N = 3$.

We assume time-harmonic fields of the form $\mathbf{E}(\mathbf{r};t) = \mathbf{E}(\mathbf{r};\omega)\exp(-i\omega t)$, where ω is the angular frequency and where the fields $\mathbf{E}(\mathbf{r};\omega)$ solve the wave equation

$$\nabla \times \nabla \times \mathbf{E}(\mathbf{r};\omega) - k_0^2 \epsilon_B(\omega)\mathbf{E}(\mathbf{r};\omega) = k_0^2 \Delta\epsilon(\mathbf{r};\omega)\mathbf{E}(\mathbf{r};\omega), \quad (1)$$

in which $k_0 = \omega/c$, c being the speed of light in free-space, and $\Delta\epsilon(\mathbf{r};\omega) \equiv \epsilon(\mathbf{r};\omega) - \epsilon_B(\omega)$ are the free-space wavenumber and the relative permittivity contrast, respectively. We suppress the explicit frequency dependence onward. The solution of Eq. (1) is the sum of the incoming field and the scattered field, giving rise to the Lippmann–Schwinger equation [17,28]

$$\mathbf{E}(\mathbf{r}) = \mathbf{E}_B(\mathbf{r}) + k_0^2 \int_{V_{\text{scat}}} \mathbf{G}_B(\mathbf{r}, \mathbf{r}')\Delta\epsilon(\mathbf{r}')\mathbf{E}(\mathbf{r}')d\mathbf{r}', \quad (2)$$

where $\mathbf{G}_B(\mathbf{r}, \mathbf{r}')$ and V_{scat} are the electromagnetic Green's tensor of the background medium and the volume of the scattering objects, respectively. The former satisfies Eq. (1) with the right-hand side replaced by $\mathbf{I}\delta(\mathbf{r} - \mathbf{r}')$, $\mathbf{I}$ being a unit dyad. The elements of the homogeneous background Green's tensor can be expressed as [14]

$$\mathbf{G}_B^{\alpha\alpha'}(\mathbf{r}, \mathbf{r}') = \left(\delta_{\alpha\alpha'} + \frac{1}{k_B^2}\partial_\alpha\partial_{\alpha'}\right)g_B(\mathbf{r}, \mathbf{r}'), \quad (3a)$$

$$g_B(\mathbf{r}, \mathbf{r}') = \frac{\exp(ik_B|\mathbf{r} - \mathbf{r}'|)}{4\pi|\mathbf{r} - \mathbf{r}'|}, \quad (3b)$$

where $g_B(\mathbf{r}, \mathbf{r}')$ and $k_B \equiv \sqrt{\epsilon_B}k_0$ are the scalar Green's function and the wavenumber of the background medium, respectively, and where $\partial_\alpha \equiv \partial/\partial\alpha$ with $\alpha, \alpha' \in \{x, y, z\}$, and $\delta_{\alpha\alpha'}$ denotes the Kronecker delta. $\mathbf{G}_B(\mathbf{r}, \mathbf{r}')$ diverges at $\mathbf{r} = \mathbf{r}'$, and since we are interested in determining the field inside the scattering objects, this singularity must be isolated. This is done using the following altered Lippmann–Schwinger equation [34]

$$\mathbf{E}(\mathbf{r}) = \mathbf{E}_B(\mathbf{r}) + k_0^2 \int_{V_{\text{scat}}-\delta V} \mathbf{G}_B(\mathbf{r}, \mathbf{r}')\Delta\epsilon(\mathbf{r}')\mathbf{E}(\mathbf{r}')d\mathbf{r}' - \mathbf{L}\frac{\Delta\epsilon(\mathbf{r})}{\epsilon_B}\mathbf{E}(\mathbf{r}). \quad (4)$$

The integral is now evaluated as a principal value, omitting the point $\mathbf{r} = \mathbf{r}'$, which is compensated by the introduction of the source dyadic $\mathbf{L}$. We choose spherical exclusion volumes δV,
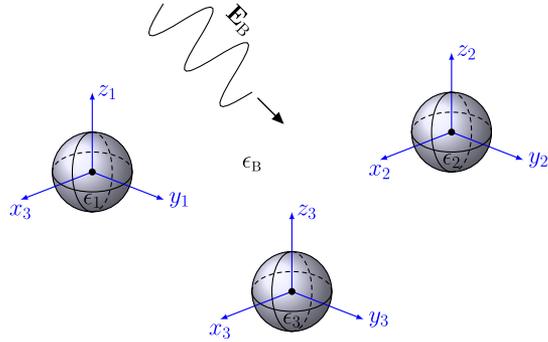
Fig. 1.   Example of scattering geometry where an incoming field, $\mathbf{E}_B$, impinges on $N = 3$ spherical scatterers embedded in a homogeneous material of permittivity ϵ_B. The scatterers have permittivities ϵ_j, and the local coordinate systems are indicated.

for which $\mathbf{L}^{\alpha\alpha'} = \delta_{\alpha\alpha'}/3$ [34]. We note that Eq. (4) is implicit for $\mathbf{r} \in V_{\text{scat}}$ and explicit for $\mathbf{r} \notin V_{\text{scat}}$. Therefore, the majority of the computational work will concern the calculation of the field inside the scatterers. Once the field is known in these regions, it is straightforward to calculate the solution at all other points. In Sections 2.B–2.E, we present the procedure for solving Eq. (4); in Section 2.F the steps in the procedure are summarized.

    If the field can be well approximated by constants inside each of the scatterers, Eq. (4) may be solved simply by pulling the field outside the integral. This transforms the implicit Lippmann–Schwinger equation into a system of algebraic equations for the $3N$ field values inside the scatterers, which may be solved directly. We refer to this approximate solution scheme as the dipole approximation (DA), and in Section 3.A we compare it to the full formalism that we develop below. Note that we take the finite extent of the scatterers into account by evaluating the integrals over the elements of the Green's tensor analytically in the DA presented here. This approach is therefore more elaborate than the well-known point-scatterer model [35] that is often employed in the literature. An extensive work on point-scatterer modeling can be found in [36].

B. Expansion of Electric Field
To solve Eq. (4) inside V_{scat}, we employ an expansion of the field and the background field inside scatterer j,

$$\mathbf{E}(\mathbf{r}_j) = \sum_{\alpha,l,m} a_{j\alpha lm}\psi_{l,m}^j(\mathbf{r}_j)\mathbf{e}_\alpha, \tag{5a}$$

$$\mathbf{E}_B(\mathbf{r}_j) = \sum_{\alpha,l,m} a_{j\alpha lm}^B\psi_{l,m}^{j,B}(\mathbf{r}_j)\mathbf{e}_\alpha, \tag{5b}$$

where $\sum_{l,m} \equiv \sum_{l=0}^\infty \sum_{m=-l}^l$, and $\mathbf{e}_\alpha$ is a unit polarization vector of the Cartesian direction α. The basis functions $\psi_{l,m}^j(\mathbf{r}_j)$ and $\psi_{l,m}^{j,B}(\mathbf{r}_j)$ are so-called spherical wave functions defined in the local coordinate system of the jth scatterer (coordinate axes in Fig. 1). These functions are defined in Appendix A and each includes a spherical harmonic, $Y_l^m(\theta_j, \phi_j)$. The parameters $a_{j\alpha lm}$ ($a_{j\alpha lm}^B$) are unknown (known) expansion coefficients, and the analysis is concerned with finding all $a_{j\alpha lm}$. We define an inner product

$$\langle f|g \rangle \equiv \int \{f(\mathbf{r})\}^Y g(\mathbf{r})d\mathbf{r}, \tag{6}$$

where $\{f(\mathbf{r})\}^Y$ implies that $f(\mathbf{r})$ is complex conjugated in the spherical harmonic only. We then have

$$\langle \psi_{l,m}^j|\psi_{l',m'}^{j'} \rangle = \delta_{jj'}\delta_{ll'}\delta_{mm'}, \tag{7a}$$

$$\langle \psi_{l,m}^{j,B}|\psi_{l',m'}^{j',B} \rangle = \delta_{jj'}\delta_{ll'}\delta_{mm'}, \tag{7b}$$

$$\langle \psi_{l,m}^j|\psi_{l',m'}^{j',B} \rangle = M_l^j\delta_{jj'}\delta_{ll'}\delta_{mm'}, \tag{7c}$$

where M_l^j is the overlap integral of two spherical Bessel functions. Inserting the expansions in Eqs. (5) into Eq. (4), projecting onto $\psi_{l,m}^j(\mathbf{r}_j)\mathbf{e}_\alpha$, and summing over all free indices produces the matrix equation

$$\mathbf{a} = \mathbf{M}_B\mathbf{a}_B + \left(k_0^2\mathbf{G}\Delta\epsilon - \frac{L}{\epsilon_B}\Delta\epsilon\right)\mathbf{a}, \tag{8}$$

where $\mathbf{a}$ and $\mathbf{a}_B$ contain the expansion coefficients of the field and the background field, respectively. $L = 1/3$ is a diagonal element of $\mathbf{L}$, while $\mathbf{M}_B$ and $\Delta\epsilon$ are diagonal matrices with diagonal elements M_l^j and $\Delta\epsilon_j \equiv \epsilon_j - \epsilon_B$, respectively. Finally, $\mathbf{G}$ is a matrix with elements of the form

$$\left[\mathbf{G}_{j,j'}^{\alpha\alpha'}\right]_{l,l'}^{m,m'} \equiv \int_{V_j}\int_{V_{j'}-\delta V}\{\psi_{l,m}^j(\mathbf{r}_j)\}^Y\mathbf{G}_B^{\alpha\alpha'}(\mathbf{r}_j,\mathbf{r}_{j'}')\psi_{l',m'}^{j'}(\mathbf{r}_{j'}')d\mathbf{r}_{j'}'d\mathbf{r}_j. \tag{9}$$

The expression for the matrix element in Eq. (9) is independent of the shape of the scattering objects. As we demonstrate in the following section, the integrals can be solved analytically for spherical scatterers, but arbitrarily shaped scatterers can in principle be handled by evaluation of the integrals in Eq. (9). This is an advantage of the use of a volume integral formulation as compared, for instance, to the generalized Mie scattering theories that rely explicitly on the spherical shape of the scatterers.

C. Green's Tensor Matrix Elements
The matrix elements in Eq. (9) fall in two classes: When $j \neq j'$, one has $r \neq r'$ by construction, and there is no need for a principal volume. Conversely, when $j = j'$ we must treat the principal volume integral with care. We term these two classes of matrix elements scattering terms and self terms, respectively.

1. Scattering Terms
Figure 2 illustrates two spherical scatterers with indices j and j'. The displacement vector between two arbitrary points inside the scatterers, $\mathbf{R}$ (dashed vector), may be expressed using the three full vectors as $\mathbf{R} = \mathbf{r}_j + \mathbf{b} - \mathbf{r}_{j'}'$. This allows an expansion of the scalar Green's function $g_B(\mathbf{r},\mathbf{r}')$ using the two-center expansion [21]

$$g_B(\mathbf{r},\mathbf{r}') = ik_B\sum_{p,t}\sum_{\nu,\mu}S_{p,\nu}^{t,\mu}(\mathbf{b})\{\tilde{\psi}_{p,t}^{j',B}(\mathbf{r}_{j'}')\}^Y\tilde{\psi}_{\nu,\mu}^{j,B}(\mathbf{r}_j), \tag{10}$$
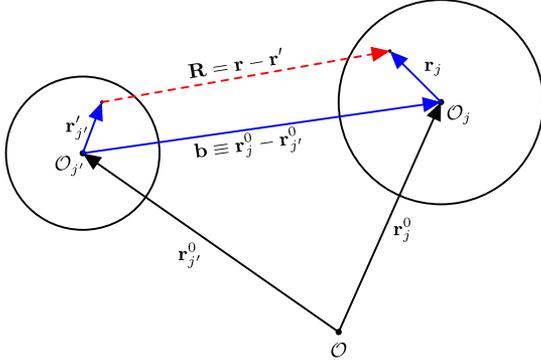
Fig. 2. Two scatterers with indices j and j', sketched in 2D. The centers of the scatterers, $\mathbf{r}_j^0$ and $\mathbf{r}_{j'}^0$, and two arbitrary local points inside the scatterers, $\mathbf{r}_j$ and $\mathbf{r}_{j'}'$, are indicated. The displacement vectors between the two points, $\mathbf{R}$, and between the centers of the scatterers, $\mathbf{b}$, are shown.

where $\tilde{\psi}_{l,m}^{j,\mathrm{B}}(\mathbf{r}_j) \equiv \psi_{l,m}^{j,\mathrm{B}}(\mathbf{r}_j)/N_l^{j,\mathrm{B}}$. The normalization constants $N_l^{j,\mathrm{B}}$ and separation matrices $S_{p,\nu}^{t,\mu}(\mathbf{b})$ are defined in Appendices A and C, respectively. In this way we have essentially represented $g_\mathrm{B}(\mathbf{r},\mathbf{r}')$ using the local background basis functions. The elements of the Green's tensor then follow from Eq. (3a) as

$$\mathbf{G}_\mathrm{B}^{\alpha\alpha'}(\mathbf{r},\mathbf{r}') = \mathrm{i}k_\mathrm{B}\sum_{p,t}\sum_{\nu,\mu}S_{p,\nu}^{t,\mu}(\mathbf{b})\{\tilde{\psi}_{p,t}^{j',\mathrm{B}}(\mathbf{r}_{j'}')\}^Y$$
$$\times\left(\delta_{\alpha\alpha'}+\frac{1}{k_\mathrm{B}^2}\partial_\alpha\partial_{\alpha'}\right)\tilde{\psi}_{\nu,\mu}^{j,\mathrm{B}}(\mathbf{r}_j). \qquad (11)$$

The Cartesian partial derivatives of the spherical wave functions may be expressed as sums of other spherical wave functions. We express this symbolically as

$$\partial_\alpha\partial_{\alpha'}\tilde{\psi}_{\nu,\mu}^{j,\mathrm{B}}(\mathbf{r}_j) = \sum_{\gamma_{\alpha,\alpha'}}g_{\gamma_{\alpha,\alpha'}}\tilde{\psi}_{\nu(\gamma_{\alpha,\alpha'}),\mu(\gamma_{\alpha,\alpha'})}^{j,\mathrm{B}}(\mathbf{r}_j), \qquad (12)$$

where $\nu(\gamma_{\alpha,\alpha'}) \equiv \nu + \gamma_{\alpha,\alpha'}'$ and $\mu(\gamma_{\alpha,\alpha'}) \equiv \mu + \gamma_{\alpha,\alpha'}''$, with $\gamma_{\alpha,\alpha'}'$ and $\gamma_{\alpha,\alpha'}''$ being integers. The sum contains a finite number of terms, and the coefficients $g_{\gamma_{\alpha,\alpha'}}$ depend both on the two polarizations α and α', and on the basis function indices ν and μ. The latter dependence, however, is suppressed for brevity. The detailed expressions for $g_{\gamma_{\alpha,\alpha'}}$ are discussed in Appendix B. Combining Eqs. (9), (11), and (12) and exploiting the orthogonality in Eq. (7c), we have an explicit expression for a generic scattering matrix element

$$\left[\mathbf{G}_{j,j'}^{\alpha\alpha'}\right]_{l,l'}^{m,m'} = \mathrm{i}k_\mathrm{B}M_l^{j'}M_l^j/(N_{l'}^{j',\mathrm{B}}N_l^{j,\mathrm{B}})$$
$$\times\left(\delta_{\alpha\alpha'}S_{l',l}^{m',m}(\mathbf{b})+\frac{1}{k_\mathrm{B}^2}\sum_{\gamma_{\alpha,\alpha'}}g_{\gamma_{\alpha,\alpha'}}S_{l',l-\gamma_{\alpha,\alpha'}'}^{m',m-\gamma_{\alpha,\alpha'}''}(\mathbf{b})\right). \qquad (13)$$

The computation of the separation matrices involved in the scattering matrix elements may be rather time consuming and in practice accounts for the majority of the computation time. These calculations, however, can be optimized [37].

2. Self Terms
To evaluate the self terms where $j = j'$, we split the $\mathbf{r}_{j'}'$ integration into two parts, in analogy with the procedure in the 2D case in [22]:

$$\left[\mathbf{G}_{j,j}^{\alpha\alpha'}\right]_{l,l'}^{m,m'} = \left[A_{j,j}^{\alpha\alpha'}\right]_{l,l'}^{m,m'} - \left[B_{j,j}^{\alpha\alpha'}\right]_{l,l'}^{m,m'}, \qquad (14)$$

where

$$\left[A_{j,j}^{\alpha\alpha'}\right]_{l,l'}^{m,m'} \equiv \int_{V_j}\int_{\mathbb{R}^3-\delta V_j}\{\psi_{l,m}^j(\mathbf{r}_j)\}^Y\mathbf{G}_\mathrm{B}^{\alpha\alpha'}(\mathbf{r}_j,\mathbf{r}_j')\psi_{l',m'}^j(\mathbf{r}_j')\mathrm{d}\mathbf{r}_j'\mathrm{d}\mathbf{r}_j, \qquad (15a)$$

$$\left[B_{j,j}^{\alpha\alpha'}\right]_{l,l'}^{m,m'} \equiv \int_{V_j}\int_{\mathbb{R}^3-V_j}\{\psi_{l,m}^j(\mathbf{r}_j)\}^Y\mathbf{G}_\mathrm{B}^{\alpha\alpha'}(\mathbf{r}_j,\mathbf{r}_j')\psi_{l',m'}^j(\mathbf{r}_j')\mathrm{d}\mathbf{r}_j'\mathrm{d}\mathbf{r}_j. \qquad (15b)$$

The integration domains for the two different cases are sketched in Fig. 3. In both cases, gray shading indicates volumes that are excluded from the $\mathbf{r}_j'$ integrations.

The left panel in Fig. 3 illustrates the integration procedure for the elements $A_{j,j}^{\alpha\alpha'}$. For any fixed $\mathbf{r}_j$, we may equally well integrate $\mathbf{R}'$ or $\mathbf{r}_j'$ over the entire space minus the principal volume. To this end, we expand $\psi_{l',m'}^j(\mathbf{r}_j')$ around $\mathbf{r}_j$ as [21]

$$\psi_{l',m'}^j(\mathbf{r}_j') = N_{l'}^j\sum_{\nu,\mu}(-1)^\mu\hat{S}_{l',\nu}^{m',\mu}(\mathbf{r}_j)\{\tilde{\psi}_{\nu,-\mu}^j(\mathbf{R}')\}^Y \qquad (16)$$

with the separation matrices $\hat{S}_{l',\nu}^{m',\mu}(\mathbf{r}_j)$ defined in Appendix C. To express the elements of the Green's tensor we write the scalar Green's function as an outgoing spherical wave function (see definition in Appendix A) as

$$g_\mathrm{B}(\mathbf{r},\mathbf{r}') = g_\mathrm{B}(\mathbf{R}') = \frac{\mathrm{i}k_\mathrm{B}}{\sqrt{4\pi}}\varphi_{0,0}^\mathrm{B}(\mathbf{R}'). \qquad (17)$$

The outgoing spherical wave functions satisfy a relation similar to Eq. (12). Using this fact, and collecting from Eqs. (15a) and (16), we may express the elements analytically as

$$\left[A_{j,j}^{\alpha\alpha'}\right]_{l,l'}^{m,m'} = \frac{\mathrm{i}k_\mathrm{B}}{\sqrt{4\pi}}N_{l'}^j\left(\delta_{\alpha\alpha'}\langle\psi_{l,m}^j|\hat{S}_{l',0}^{m',0}\rangle I_0^{\mathbb{R}^3-\delta V_j}+\frac{1}{k_\mathrm{B}^2}\sum_{\gamma_{\alpha,\alpha'}}g_{\gamma_{\alpha,\alpha'}}(-1)^{\gamma_{\alpha,\alpha'}''}\right.$$
$$\left.\times\langle\psi_{l,m}^j|\hat{S}_{l',\gamma_{\alpha,\alpha'}'}^{m',-\gamma_{\alpha,\alpha'}''}\rangle I_{\gamma_{\alpha,\alpha'}'}^{\mathbb{R}^3-\delta V_j}\right), \qquad (18)$$

where the integral $I_l^{\mathbb{R}^3-\delta V_j}$ is defined and expressed in Appendix D.
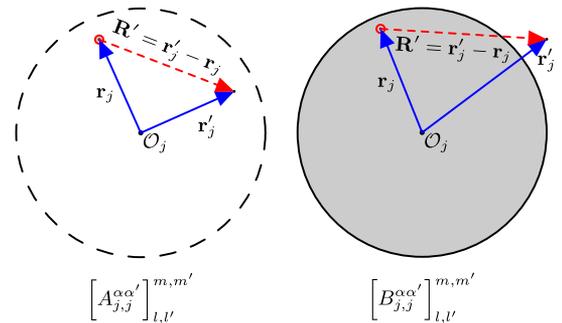
Fig. 3. Integration domains for evaluation of self terms. Gray shading indicates a volume that is excluded from the $\mathbf{r}_j'$ integration. Left panel: integration domain for $A_{j,j}^{\alpha\alpha'}$, extending over all space minus the principal volume. Right panel: integration domain for $B_{j,j}^{\alpha\alpha'}$, extending over all space minus the scatterer volume.

For the elements $B_{jj}^{\alpha\alpha'}$, by construction we have $|\mathbf{r}_j| < |\mathbf{r}_j'|$, as illustrated in the right panel in Fig. 3. Therefore, the singularity of the Green's tensor is never crossed, and we may readily expand the scalar Green's function as [21]

$$g_{\mathrm{B}}(\mathbf{R}') = ik_{\mathrm{B}}\sum_{\nu,\mu}\tilde{\psi}_{\nu,\mu}^{j,\mathrm{B}}(\mathbf{r}_j)\{\varphi_{\nu,\mu}^{\mathrm{B}}(\mathbf{r}_j')\}^Y. \tag{19}$$

Using this expansion to express the elements of the Green's tensor, we may write the elements $B_{jj}^{\alpha\alpha'}$ in closed form as

$$\left[B_{jj}^{\alpha\alpha'}\right]_{l,l'}^{m,m'} = ik_{\mathrm{B}}M_l^j I_{l'}^{\mathbb{R}^3-V_j}N_{l'}^j/(N_l^{j,\mathrm{B}})$$
$$\times \left(\delta_{\alpha\alpha'}\delta_{ll'}\delta_{mm'} + \frac{1}{k_{\mathrm{B}}^2}\sum_{\gamma_{\alpha,\alpha'}}g_{\gamma_{\alpha,\alpha'}}\delta_{l-\gamma_{\alpha,\alpha'}',l'}\delta_{m-\gamma_{\alpha,\alpha'}'',m'}\right), \tag{20}$$

where $I_{l'}^{\mathbb{R}^3-V_j}$ is defined and expressed in Appendix D. We refer to Appendix B for details of the sum $\sum_{\gamma_{\alpha,\alpha'}}g_{\gamma_{\alpha,\alpha'}}$.

D. Field Outside Scatterers
Having determined the electric field inside the scattering objects, the Lippmann–Schwinger equation is explicit for the field at positions outside the scatterers, for which we find

$$\mathbf{E}^\alpha(\mathbf{r}) = \mathbf{E}_{\mathrm{B}}^\alpha(\mathbf{r}) + k_0^2\sum_{j=1}^N\Delta\epsilon_j\sum_{\alpha'}H_j^{\alpha\alpha'}(\mathbf{r}), \tag{21a}$$

$$H_j^{\alpha\alpha'}(\mathbf{r}) \equiv \int_{V_j}\mathbf{G}_{\mathrm{B}}^{\alpha\alpha'}(\mathbf{r},\mathbf{r}_j')\mathbf{E}^{\alpha'}(\mathbf{r}_j')\mathrm{d}\mathbf{r}_j'. \tag{21b}$$

The integrals $H_j^{\alpha\alpha'}(\mathbf{r})$ can be evaluated analytically following a procedure similar to the evaluation of $B_{jj}^{\alpha\alpha'}$, as discussed in Section 2.C.2.

E. Background Field
To solve Eq. (8) for $\mathbf{a}$ we need the expansion coefficients of the background field, $\mathbf{a}_{\mathrm{B}}$; cf. Eq. (5b). In the following sections, we list these coefficients for different types of excitations.

1. Plane Wave
We consider an incoming plane wave of the form

$$\mathbf{E}_{\mathrm{B}}(\mathbf{r}) = E_0\,\exp(i\mathbf{k}_{\mathrm{B}}\cdot\mathbf{r})\mathbf{e}_{\mathrm{B}}, \tag{22}$$

where $\mathbf{k}_{\mathrm{B}}$ and $\mathbf{e}_{\mathrm{B}}$ are the wave vector and the unit polarization vector, respectively, satisfying $\mathbf{k}_{\mathrm{B}}\cdot\mathbf{e}_{\mathrm{B}} = 0$. The expansion coefficients of this field on the background spherical wave functions are [21]

$$a_{j\alpha lm}^{\mathrm{B}} = [E_0\mathbf{e}_{\mathrm{B}}^\alpha 4\pi i^l\{Y_l^m(\theta_k,\phi_k)\}^*/(N_l^{j,\mathrm{B}})]\exp(i\mathbf{k}_{\mathrm{B}}\cdot\mathbf{r}_j^0), \tag{23}$$

where θ_k and ϕ_k are the polar and azimuthal angles of $\mathbf{k}_{\mathrm{B}}$, respectively.

2. Dipole Emitter—Background Green's Tensor
The Green's tensor $\mathbf{G}(\mathbf{r},\mathbf{r}')$ is proportional to the electric field at the point $\mathbf{r}$ produced by three dipoles, with dipole moments along $\alpha \in \{x,y,z\}$, positioned at $\mathbf{r}'$. Consequently, we determine $\mathbf{G}(\mathbf{r},\mathbf{r}')$ by using the homogeneous background medium Green's tensor $\mathbf{G}_{\mathrm{B}}(\mathbf{r},\mathbf{r}')$ as the background field in the Lippmann–Schwinger equation [28]. To that end, we need an expansion of the background Green's tensor on the background basis functions. As shown in Appendix E, the expansion coefficients are

$$a_{j\alpha lm}^{\mathrm{B}} = ik_{\mathrm{B}}(-1)^m/(N_l^{j,\mathrm{B}})\bigg(\delta_{\alpha\alpha'}\varphi_{l,-m}^{\mathrm{B}}(\mathbf{r}_j')$$
$$+ \frac{1}{k_{\mathrm{B}}^2}\sum_{\gamma_{\alpha,\alpha'}}g_{\gamma_{\alpha,\alpha'}}\varphi_{l(\gamma_{\alpha,\alpha'}),m^*(\gamma_{\alpha,\alpha'})}^{\mathrm{B}}(\mathbf{r}_j')\bigg). \tag{24}$$

From $\mathbf{G}(\mathbf{r},\mathbf{r}')$, the projected LDOS of the dipole emitter may readily be obtained as [14]

$$\rho^\alpha(\mathbf{r};\lambda_0) = \frac{4}{c\lambda_0}\,\mathrm{Im}(\mathbf{G}^{\alpha\alpha}(\mathbf{r},\mathbf{r})). \tag{25}$$

Since, in general, $\rho^\alpha(\mathbf{r};\lambda_0)$ is different for different orientations of the emitter, α, Eq. (25) is in fact a projected LDOS. Nevertheless in the remainder of the article we shall refer to Eq. (25) simply as the LDOS. The LDOS gives the number of modes per unit volume and frequency that the emitter can decay spontaneously into, and an important figure of merit is therefore the relative enhancement of the LDOS, $\rho^\alpha(\mathbf{r};\lambda_0)/\rho_{\mathrm{B}}^\alpha(\lambda_0)$, due to the presence of the scattering objects. The relative LDOS is known also as the Purcell factor F_{P} [30]. As an example, we compute this quantity for a plasmonic dimer in Section 3.B. Assuming that emissions from the individual dipoles are independent, we may include several dipole emitters at distinct positions by summing over the expansion coefficients in Eq. (24), with different $\mathbf{r}_j'$ for each dipole emitter. An example of such a calculation, with a single spherical scattering object, is presented in [38]. In this case, however, the resulting field does not represent the Green's tensor.

3. No Background Field—Quasi-normal Modes
The formalism of this work treats open systems where no boundaries enclose the structures. The modes of such open systems are inherently leaky and appear as solutions of non-Hermitian eigenvalue problems that give rise to complex eigenfrequencies $\tilde{\omega}_i$. These modes are referred to as quasi-normal modes [39]. The quasi-normal modes $\mathbf{f}_i(\mathbf{r};\tilde{\omega}_i)$ may be determined as self-consistent solutions of an "excitation-free" Lippmann–Schwinger equation [32],

$$\mathbf{f}_i(\mathbf{r};\tilde{\omega}_i) = k_0^2(\tilde{\omega}_i)\int_V\mathbf{G}_{\mathrm{B}}(\mathbf{r},\mathbf{r}';\tilde{\omega}_i)\Delta\epsilon(\mathbf{r}';\tilde{\omega}_i)\mathbf{f}_i(\mathbf{r}';\tilde{\omega}_i)\mathrm{d}\mathbf{r}'. \tag{26}$$

In the above, we have absorbed the technical detail of the source dyadic in the integral for brevity. Likewise, we have written the frequency dependence explicitly, and using the expansion technique developed in the previous sections and an iteration of the eigenfrequencies, we determine the quasi-normal modes by solving Eq. (26) self-consistently. Due to their leaky nature, the quasi-normal modes give rise to finite Q factors [14] that we can calculate as $Q_i = -\mathrm{Re}(\tilde{\omega}_i)/(2\,\mathrm{Im}(\tilde{\omega}_i))$.

F. Summary of Formalism

We summarize the steps in the procedure for solving Eq. (4):

1. We expand each component of the total electric field $\mathbf{E}(\mathbf{r})$ and the incoming field $\mathbf{E}_B(\mathbf{r})$ inside each of the N scatterers on orthonormal sets of basis functions in Eqs. (5).

2. The expansions are inserted into Eq. (4), projected onto an arbitrary basis function, and summed over all free indices to yield the matrix equation for the expansion coefficients of the total electric field $\mathbf{a}$ in Eq. (8).

3. The matrices in Eq. (8) are calculated: The diagonal matrices $\mathbf{M}_B$ and $\Delta\epsilon$ are constructed directly by means of the orthonormality of the basis functions in Eqs. (7). The non-diagonal matrix $\mathbf{G}$ is evaluated using a number of expansions of the Green's tensor as discussed in Section 2.C.

4. The incoming field is expanded. Examples for several types of excitation fields are given in Section 2.E.

5. We finally solve Eq. (8) for the expansion coefficients $\mathbf{a}$.

Subsequently, depending on the choice of incoming field, derived quantities at positions outside the scatterers may be calculated straightforwardly using Eqs. (21).

G. Far-Field Radiation Pattern and Extinction Cross Section

The scattered field, that is, the second term on the right-hand side of Eq. (2), must satisfy the radiation BC in the far-field [18],

$$\mathbf{E}_{\text{scat}}(\mathbf{r}) \sim \mathbf{f}(\theta, \phi) E_0 \frac{\exp(i k_B r)}{r}, \qquad 1 \ll k_B r, \qquad (27)$$

where $\mathbf{f}(\theta, \phi)$ is the far-field radiation pattern at the polar and azimuthal angles, θ and ϕ, of $\mathbf{r}$. The scattered field outside the scattering objects is represented by the second term on the right-hand side of Eq. (21a), and these terms are all proportional to a spherical Hankel function of the first kind $h_l^{(1)}(k_B r)$. Expanding these functions asymptotically as [40],

$$h_l^{(1)}(k_B r) \sim \frac{(-i)^{l+1}}{k_B} \frac{\exp(i k_B r)}{r}, \qquad 1 \ll k_B r, \qquad (28)$$

and using the definition of the far-field radiation pattern in Eq. (27), we may write $\mathbf{f}(\theta, \phi)$ analytically.

The extinction cross section is defined as the power removed from an incoming plane wave, P, relative to the magnitude of the incoming Poynting vector, $C_{\text{ext}} \equiv P/|\mathbf{S}_B|$. P can be computed by brute force evaluation of the energy flux through a sphere enclosing the scattering objects but may be more elegantly expressed using the optical theorem [18,27] as

$$C_{\text{ext}} = \frac{4\pi}{k_B} \text{Im}(\mathbf{f}(\theta_k, \phi_k) \cdot \mathbf{e}_B^*). \qquad (29)$$

The extinction cross section C_{ext} has the dimension of area and can be interpreted as an equivalent area over which the incoming radiation interacts with the scattering objects. It is therefore customary to normalize it to the geometric cross section, giving rise to the extinction efficiency $Q_{\text{ext}} \equiv C_{\text{ext}}/(N\pi R^2)$, where R is the radius of each of the N spheres.

H. Error Estimate

As discussed in [22], the Lippmann–Schwinger equation provides a direct error estimate of the computed field. Rearranging Eq. (4), we may define the local error at a point $\mathbf{r}$ inside a scattering object as

$$\mathcal{E}_L(\mathbf{r}) \equiv \left| \mathbf{E}_B(\mathbf{r}) - \mathbf{E}(\mathbf{r}) - \mathbf{L} \frac{\Delta\epsilon(\mathbf{r})}{\epsilon_B} \mathbf{E}(\mathbf{r}) \right.$$
$$\left. + k_0^2 \int_{V_{\text{scat}}-\delta V} \mathbf{G}_B(\mathbf{r}, \mathbf{r}') \Delta\epsilon(\mathbf{r}') \mathbf{E}(\mathbf{r}') d\mathbf{r}' \right|. \qquad (30)$$

In this expression, $\mathbf{E}(\mathbf{r})$ is the approximation to the electric field, that is, Eq. (5a) with a finite number of basis functions retained. We also define the global relative error

$$\mathcal{E}_G \equiv \frac{\int_{V_{\text{scat}}} \mathcal{E}_L(\mathbf{r}) d\mathbf{r}}{\int_{V_{\text{scat}}} |\mathbf{E}(\mathbf{r})| d\mathbf{r}}, \qquad (31)$$

which represents an explicit error estimate of the field. In practice, the set of basis functions is truncated by truncating l at l_{max}, and a specific calculation of $\mathcal{E}_G$ is presented in Section 3.A. In the case of spherical scatterers, as considered in this work, all matrix elements are expressed analytically, and the truncation of the set of basis functions therefore represents the most significant approximation in the formalism.

3. EXAMPLE CALCULATIONS: PLASMONIC DIMER

It is well known that metallic nanoparticles may sustain collective oscillations of free charges known as plasmons. A special type of plasmon is LSPs, bound to the interface between a metal and a dielectric, that give rise to strongly enhanced near-fields [41]. The plasmonic dimer that we examine in the following sections may support LSPs, and it has been demonstrated that the resonance wavelengths of these depend sensitively on parameters such as the distance between the particles and their sizes [6]. The LSP occurring at the largest excitation wavelength is known as the dipole LSP [42,43], while resonances at shorter wavelengths are higher-order LSPs. It has been shown that the dipole resonance redshifts or blueshifts for decreasing distance between the metal nanoparticles for parallel or perpendicular polarization (with respect to the dimer axis) of the incoming field, respectively [44]. For parallel polarization, it has been suggested that the relative shift of the resonance wavelength for the dimer depends exponentially on the gap distance between the particles. This analysis was based on a qualitative description for the dimer as an electric dipole [45]. For gap sizes below the radius of the particles, however, the strong coupling of the near-fields between the particles makes this simple description invalid [46], and modeling including higher-order wavefunctions, as in the present approach, is needed to correctly analyze the closely spaced nanoparticles.

The dimer consists of two Ag particles aligned along the y axis, each of radius $R = 25$ nm and spaced a distance d apart, as shown in Fig. 4. In all calculations, $R = 25$ nm is fixed while d is a parameter. The particles are embedded in SiO_2 ($\epsilon_B = 2.25$), and the permittivity of the Ag spheres is given by the Drude model $\epsilon(\omega) = 1 - \omega_p^2/(\omega^2 + i\gamma\omega)$ with $\hbar\omega_p = 7.9$ eV and $\hbar\gamma = 0.06$ eV [47].
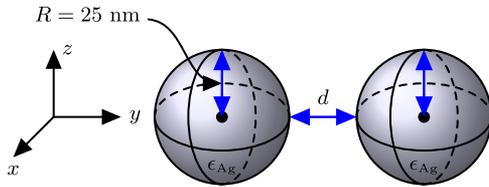
Fig. 4.   Schematic of plasmonic dimer consisting of two Ag spheres aligned along the y axis. Each particle has radius $R = 25$ nm, and the surface-to-surface distance between the spheres is d.

A. Plane Wave Scattering

We illuminate the dimer by plane waves polarized parallel ($\mathbf{e}_\mathrm{B} = \hat{y}$) or perpendicular ($\mathbf{e}_\mathrm{B} = \hat{x}$) to the dimer axis. In both cases, the incoming field propagates perpendicularly to the dimer axis ($\mathbf{k}_\mathrm{B} = k_\mathrm{B}\hat{z}$).

Two LSPs excited by the plane waves are displayed in Fig. 5, showing the relative enhancement of the electric field intensity in a log-scale, in the x–y plane at $z = 0$. The distance between the spheres is $d = 10$ nm. The maximum relative intensity enhancement is roughly an order of magnitude larger for parallel than for perpendicular polarization. For parallel polarization the enhancement occurs in the gap, while for perpendicular polarization maximum enhancement occurs at the surfaces of the particles. This is caused by the charge oscillations in the metal particles that move in phase with the exciting field [45]. In the parallel case, this produces a charge difference across the gap, which gives an enhanced field between the particles, while in the perpendicular case the charge distributions give strongly enhanced fields on the individual particles.

Figure 6 shows the extinction efficiency spectrum for a dimer with spacing $d = 50$ nm that is excited by parallel
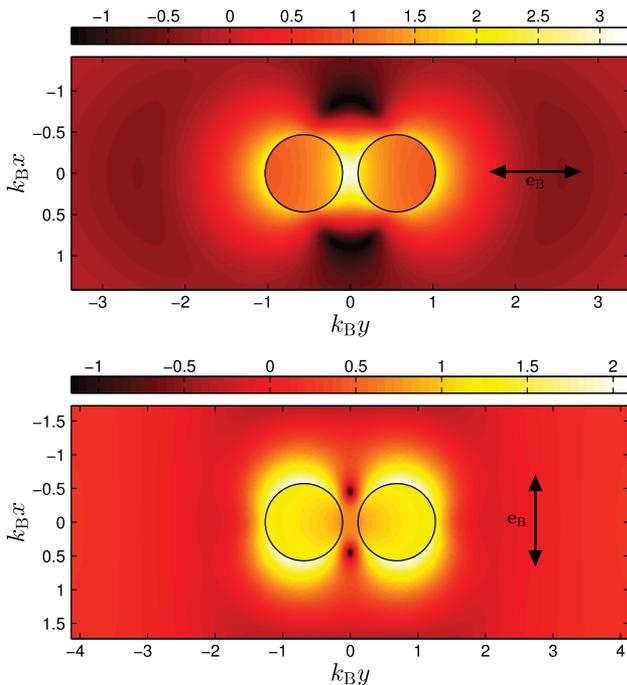
Fig. 5.   Relative enhancement of the electric field intensity, $\log_{10}(|\mathbf{E}|^2/|\mathbf{E}_\mathrm{B}|^2)$, for scattering of a plane wave on a dimer, shown in the x–y plane at $z = 0$. The spacing between the particles is $d = 10$ nm. The incoming plane wave propagates along the z direction and is polarized parallel (top panel, $\lambda_0 = 505$ nm) or perpendicular (bottom panel, $\lambda_0 = 412$ nm) to the dimer axis. Note that different color scales are used in the two plots.
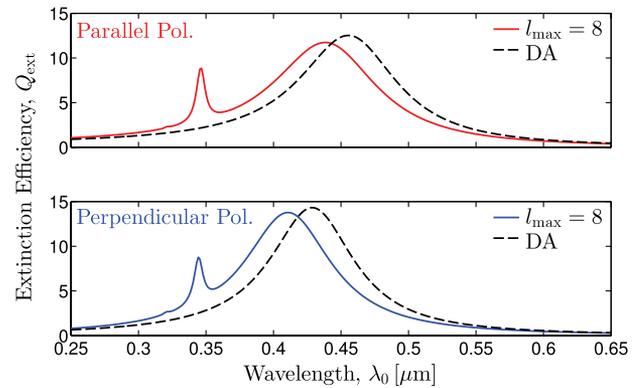
Fig. 6.   Extinction efficiency Q_{ext} versus excitation wavelength for scattering of a plane wave on two Ag spheres spaced by $d = 50$ nm. The incoming field is polarized parallel (top panel) or perpendicular (bottom panel) to the dimer axis. The spectra have been obtained using the full formalism with $l_{\max} = 8$ and the DA.

(top panel) and perpendicular (bottom panel) plane waves. The spectra are computed using the full formalism developed in Section 2 ($l_{\max} = 8$, full curves) and using the DA (dashed). We have also computed the spectra using $l_{\max} = 10$, and comparing these with the $l_{\max} = 8$ spectra we find a vanishing relative deviation on the dipole resonance wavelength for both polarizations and a relative deviation on the resonance values of $\sim 10^{-13}$. The spectra obtained using the full formalism and using the DA look qualitatively the same: They predict the dipole resonances at $\lambda_0 \sim 450$ nm and at $\lambda_0 \sim 425$ nm in the parallel and perpendicular cases, respectively. The relative deviations of the DA calculations for the dipole resonance wavelengths are in both cases 4%, while the relative deviation, on resonance, of the extinction efficiency is 7% and 4%, respectively. These relative errors increase for decreasing spacing d (not shown), illustrating the limitation of the DA for closely spaced nanoparticles. Another shortcoming of the DA is that it is inherently monomode; it only predicts the dipole resonance and not the higher-order mode occurring at $\lambda_0 \sim 340$ nm. In line with the DA, the quasi-static approximation is another popular approximate scheme for solving Eq. (1). In [48], Chen *et al.* analyzed the electrodynamic coupling between a quantum dot and a plasmonic nanowire. In particular, it was demonstrated that the characteristic size of the scatterer (plasmonic nanowire) needs to be smaller than the skin depth of the metal for the quasi-static approximation to accurately model the coupling. The results in Fig. 6 and in [48] demonstrate the need for full vectorial solvers for modeling nanoplasmonic structures when these contain small features, such as small spacings as in the example of this section.

To further investigate the impact of truncating the basis set, Fig. 7 shows the global relative error $\mathcal{E}_\mathrm{G}$ of the electric field for the dimer as a function of d/R and for three values of $l_{\max}$. The system is illuminated by a plane wave as detailed in the caption of the figure. At the largest spacing, $d/R = 30$, the global relative error decreases by five to six orders of magnitude when $l_{\max}$ increases by three units. As d/R decreases, the global relative error increases for fixed $l_{\max}$. This reduction in accuracy is caused by the introduction of an increasingly smaller length scale, namely the distance between the particles, and more basis functions are needed to resolve this correctly. As an example, with $l_{\max} = 2$ and for $d/R = 1$ and $d/R = 0.5$ the global relative errors equal 36% and 80%,
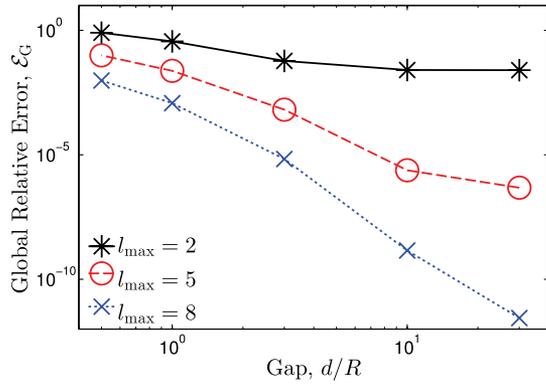
Fig. 7. Global relative error of the electric field as a function of distance between two Ag spheres, d/R. Results for three different truncations of the set of basis functions are shown. Illumination by plane waves at $\lambda_0 = 800$ nm with oblique incidence and polarization.

respectively, which supports the conclusion that vectorial solvers are needed to correctly model closely spaced nanoparticles. Similar results were obtained using a different solution technique in [46]. We note that in the limit $d/R \ll 1$, nonlocal effects [49] become important and must be included to correctly model the field. For fixed particle distance, the exponential decay of the relative error in Fig. 7 enables highly accurate calculations with a modest number of basis functions, and in the following sections we use $l_{\max} = 8$.

B. Dipole Emitter and LDOS

We embed a dipole emitter with dipole moment along the direction α in the vicinity of the plasmonic dimer. The field radiated by the emitter equals the αth column of the Green's tensor $\mathbf{G}(\mathbf{r}, \mathbf{r}')$ where $\mathbf{r}'$ is the dipole position. Figure 8 shows the imaginary part of the Green's tensor $\mathrm{Im}(\mathbf{G}^{yy}(\mathbf{r}, \mathbf{r}'))$ relative to $\mathrm{Im}(\mathbf{G}_{\mathrm{B}}^{yy}(\mathbf{r}', \mathbf{r}'))$ for two positions of the dipole $\mathbf{r}'$ (indicated by dots in the figure) and at two different wavelengths, $\lambda_0 = 505$ nm (top panel) and $\lambda_0 = 447$ nm (bottom panel). In the top panel, the imaginary part of the Green's tensor is strongly enhanced relative to the background Green's tensor at the position of the emitter. Conversely, the imaginary part of the Green's tensor is not enhanced at the emitter position in the bottom panel. From the expression for the LDOS in Eq. (25) we know that the LDOS is proportional to the imaginary part of the Green's tensor at the emitter position. To further investigate the emission properties of the dipole emitter, we analyze the Purcell factor in the following.

We compute the Purcell factor for two orientations of the dipole moment, $\alpha \in \{x, y\}$, and at the two positions from Fig. 8, producing the spectra in Fig. 9. At the symmetric position $\mathbf{r} = \mathbf{r}_1$ (top panel), the Purcell factor has a single peak at $\lambda_0 \sim$ 290 nm for an x-oriented dipole (full curve). In contrast, for a dipole moment along the dimer axis, $\alpha = y$ (dashed curve), the Purcell factor is larger than unity over most of the considered wavelength range, 280 nm $\lesssim \lambda_0$ and exhibits a maximum at $\lambda_0 \sim 505$ nm, resulting in the enhancement that was noted in the discussion of the top panel in Fig. 8. At the asymmetric position $\mathbf{r} = \mathbf{r}_2$ (bottom panel), the Purcell factor is generally smaller than at $\mathbf{r} = \mathbf{r}_1$. For x orientation of the dipole (full curve), the Purcell factor is larger than unity in the range 290 nm $\lesssim \lambda_0 \lesssim 500$ nm and exhibits multiple peaks in this range. For a dipole moment along the dimer axis, $\alpha = y$ (dashed curve), the Purcell factor is larger than one in a
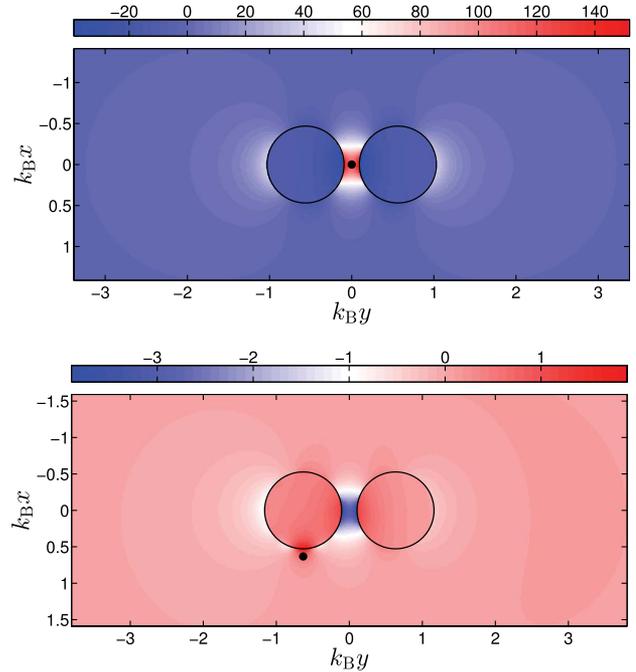
Fig. 8. Imaginary part of Green's tensor $\mathrm{Im}(\mathbf{G}^{yy}(\mathbf{r}, \mathbf{r}'))$ relative to $\mathrm{Im}(\mathbf{G}_{\mathrm{B}}^{yy}(\mathbf{r}', \mathbf{r}'))$ for the dimer with two Ag spheres ($d/R = 0.4$). The two panels show results with different positions of the dipole emitter, $\mathbf{r}'$, (black dots) and different wavelengths $\lambda_0 = 505$ nm (top) and $\lambda_0 = 447$ nm (bottom). Note that different color scales are used in the two plots.

narrow bandwidth, 300 nm $\lesssim \lambda_0 \lesssim 350$ nm, but is otherwise suppressed, in particular at $\lambda_0 \sim 447$ nm in agreement with the discussion of the bottom panel in Fig. 8. In conclusion, the results in Fig. 9 show a rich display of peaks, each of which we can associate with a quasi-normal mode of the dimer. In the following section, we focus on two of these as noted in Fig. 9.

C. Bright and Dark Modes

The dimer introduced in Fig. 9 was analyzed by Koenderink in [47], using the method of [26]. In particular, Koenderink found a mode of that structure with a quality factor of $Q = 5.7$ at $\lambda_0 \sim 506$ nm. However, no rigorous definition of the mode was given. The plasmonic dimer supports both bright and dark quasi-normal modes; the former can be excited both from the far-field (plane waves) and the near-field (dipole emitter),
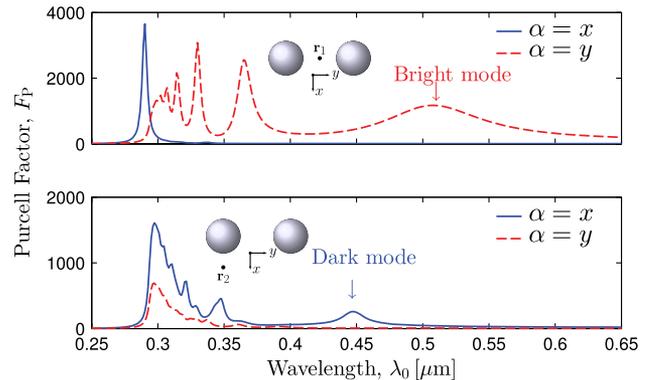
Fig. 9. Spectra of Purcell factor for dipole emitter at two positions, $\mathbf{r}_1$ (top panel) and $\mathbf{r}_2$ (bottom panel), in the $z = 0$ plane in the vicinity of the Ag dimer with $d/R = 0.4$. Two orientations of the dipole moment of the emitter, $\alpha \in \{x, y\}$, have been employed. Note that different scalings are used in the two plots.
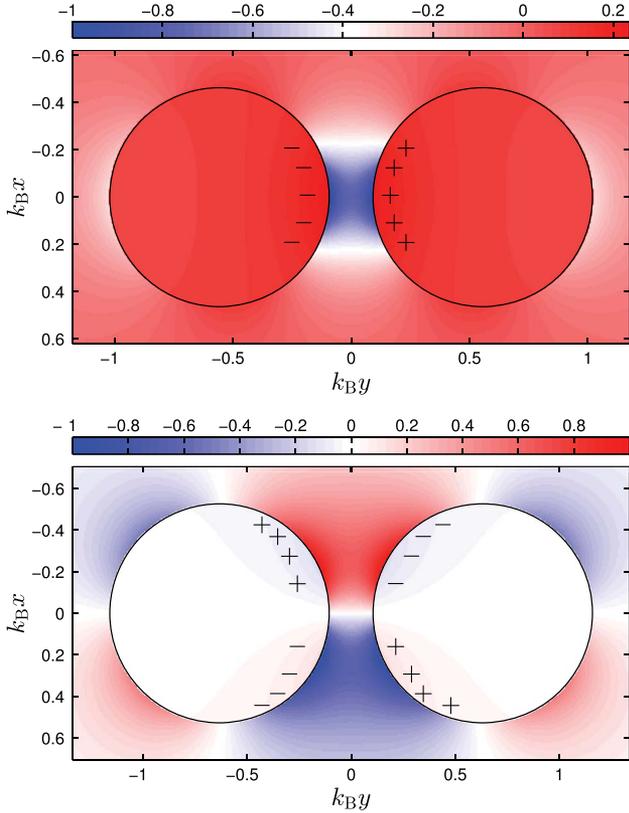
Fig. 10.   Real part of y components of quasi-normal modes of plasmonic dimer, as specified in Fig. 9, in the x–y plane. The modes, found at $\mathrm{Re}(\lambda_0^{\mathrm{bright}}) = 505$ nm (top panel) and $\mathrm{Re}(\lambda_0^{\mathrm{dark}}) = 447$ nm (bottom panel), respectively, are bright and dark modes, respectively. Note that different scalings are used in the two plots.

while the latter can only be excited from the near-field [50]. Each of the peaks in the Purcell factor spectra correspond to the existence of a quasi-normal mode. For the dimer of Fig. 9, we find two of the lowest order modes at $\mathrm{Re}(\lambda_0^{\mathrm{bright}}) = 505$ nm and $\mathrm{Re}(\lambda_0^{\mathrm{dark}}) = 447$ nm, as indicated in the figure, with low quality factors of $Q^{\mathrm{bright}} = 5.7$ and $Q^{\mathrm{dark}} = 22.1$, respectively. The bright mode is the mode that Koenderink found, demonstrating a quantitative agreement between our method and that of [26].

Figure 10 shows the real parts of the y components of the two modes in the x–y plane; the top and the bottom panels show the bright and the dark mode, respectively. In the two cases, the surface charge distributions that act to sustain the modes are indicated schematically. The bright mode is uniform in the gap between the particles due to the charge difference across the gap. This charge distribution gives rise to a finite dipole moment of the dimer which is excitable by incoming plane waves. In contrast, due to the asymmetry in the charge distribution the dark mode changes sign inside the gap, as shown in the figure. This charge distribution implies a zero net dipole moment of the mode, and consequently it is *not* excitable by plane waves.

4. CONCLUSION

We have developed a formalism for solving the Lippmann–Schwinger equation for the electric field in a 3D background medium with inhomogeneities. We have in detail explained the solution procedure for the specific example of spherical

scattering objects, and based on expansions in spherical wave functions and addition and translation theorems we have expressed all parts of the formalism analytically. We stress that other shapes of the scatterers as well as inhomogeneous background media can be treated within the presented framework, although it may not be possible to express the matrix elements analytically. We have presented an explicit error estimate for the calculated electric field and illustrated how this is an important tool for assessing the accuracy of the calculations. Using the formalism, we have shown how to calculate a number of physically important quantities, including the far-field radiation pattern, the extinction cross section, the total Green's tensor, the projected LDOS, the Purcell factor, and quasi-normal modes with their associated Q factors. In particular, the analysis of LSPs as quasi-normal modes provides additional physical insights, and we believe that more complex structures can benefit from this modal approach. Similar analyses of more complicated systems such as larger arrays of plasmonic nanoparticles or photonic crystals can readily be carried out; see [33] for an example.

We believe that the versatility of the formalism will be useful for a variety of computational problems within nanophotonics. The formulation may benefit from known expressions for the background Green's tensor for different background media, for instance for modeling of layered 3D structures [20]. As another perspective, we mention that the present formalism may be used for simulating electron energy loss spectroscopy (EELS) on plasmonic nanospheres. The incoming electron beam in EELS gives rise to a background electric field, and expanding this field on the background basis functions [51], the EELS field may be straightforwardly determined with the formalism developed in this paper.

APPENDIX A: SPHERICAL WAVE FUNCTIONS

The basis functions used in the expansions in Eqs. (5) are defined as follows:

$$\psi_{l,m}^{j}(\mathbf{r}_j) \equiv S_j(\mathbf{r})N_l^j j_l(k_j r_j)Y_l^m(\theta_j, \phi_j), \qquad (\text{A1a})$$

$$\psi_{l,m}^{j,\mathrm{B}}(\mathbf{r}_j) \equiv S_j(\mathbf{r})N_l^{j,\mathrm{B}} j_l(k_\mathrm{B} r_j)Y_l^m(\theta_j, \phi_j), \qquad (\text{A1b})$$

where

$$S_j(\mathbf{r}) \equiv \begin{cases} 1 & \mathbf{r} \in V_j \\ 0 & \text{otherwise} \end{cases}, \qquad (\text{A2})$$

ensures that basis functions of different scatterers are orthogonal by construction. N_l^j and $N_l^{j,\mathrm{B}}$ are normalization constants, determined to satisfy Eqs. (7a) and (7b), and $k_j \equiv \sqrt{\epsilon_j}k_0$ and k_B are the wavenumbers of the jth scatterer and of the background medium, respectively. Finally, $j_l(x)$ and $Y_l^m(\theta, \phi)$ are the spherical Bessel function of order l and the spherical harmonic of degree l and order m, respectively; these functions follow the conventions of [21].

For representing the scalar Green's function, $g_\mathrm{B}(\mathbf{r}, \mathbf{r}')$, we introduce the outgoing spherical wave functions:

$$\varphi_{l,m}^{\mathrm{B}}(\mathbf{r}) \equiv h_l^{(1)}(k_\mathrm{B} r)Y_l^m(\theta, \phi), \qquad (\text{A3})$$

where $h_l^{(1)}(k_{\mathrm{B}}r_j)$ is a spherical Hankel function of the first kind.

APPENDIX B: DERIVATIVES OF SPHERICAL WAVE FUNCTIONS

We define the following functions:

$$\tilde{\psi}_{l,m}^j(\mathbf{r}_j) \equiv \frac{\psi_{l,m}^j(\mathbf{r}_j)}{N_l^j}, \tag{B1a}$$

$$\tilde{\psi}_{l,m}^{j,\mathrm{B}}(\mathbf{r}_j) \equiv \frac{\psi_{l,m}^{j,\mathrm{B}}(\mathbf{r}_j)}{N_l^{j,\mathrm{B}}}, \tag{B1b}$$

and let $\Omega_l^m(\mathbf{r})$ be any of these functions or the outgoing spherical wave functions

$$\Omega_l^m(\mathbf{r}) \in \left\{ \tilde{\psi}_{l,m}^j(\mathbf{r}_j), \tilde{\psi}_{l,m}^{j,\mathrm{B}}(\mathbf{r}_j), \varphi_{l,m}^{\mathrm{B}}(\mathbf{r}) \right\}. \tag{B2}$$

We also define the following differential operators [21]:

$$\mathcal{D}_1^{\pm} \equiv -\frac{1}{k}(\partial_x \pm i\partial_y), \tag{B3a}$$

$$\mathcal{D}_1^0 \equiv -\frac{1}{k}\partial_z, \tag{B3b}$$

where k is k_j for $\tilde{\psi}_{l,m}^j(\mathbf{r}_j)$ and k_{B} for $\tilde{\psi}_{l,m}^{j,\mathrm{B}}(\mathbf{r}_j)$ and $\varphi_{l,m}^{\mathrm{B}}(\mathbf{r})$.

The action of these differential operators on $\Omega_l^m(\mathbf{r})$ can be expressed as [21]

$$\mathcal{D}_1^{\pm}\Omega_l^m(\mathbf{r}) = \mp\left(\sqrt{\frac{(l\pm m+2)(l\pm m+1)}{(2l+1)(2l+3)}}\Omega_{l+1}^{m\pm 1}(\mathbf{r})\right.$$
$$\left. + \sqrt{\frac{(l\mp m)(l\mp m-1)}{4l^2-1}}\Omega_{l-1}^{m\pm 1}(\mathbf{r})\right), \tag{B4a}$$

$$\mathcal{D}_1^0\Omega_l^m(\mathbf{r}) = \sqrt{\frac{(l+1)^2-m^2}{(2l+1)(2l+3)}}\Omega_{l+1}^m(\mathbf{r}) - \sqrt{\frac{l^2-m^2}{4l^2-1}}\Omega_{l-1}^m(\mathbf{r}). \tag{B4b}$$

Combining Eqs. (B3) and (B4), the detailed expressions for $\partial_\alpha\partial_{\alpha'}\tilde{\psi}_{\nu,\mu}^{j,\mathrm{B}}(\mathbf{r}_j)$, for example, may be obtained.

APPENDIX C: SEPARATION MATRICES

The separation matrix, $S_{p,\nu}^{t,\mu}(\mathbf{b})$, introduced in Eq. (10), can be expressed as follows [21]:

$$S_{p,\nu}^{t,\mu}(\mathbf{b}) = 4\pi(-1)^{\nu+\mu+Q}\sum_{q=0}^Q (-1)^q \varphi_{q_0+2q,t-\mu}^{\mathrm{B}}(\mathbf{b})$$
$$\times \mathcal{G}(p,t;\nu,-\mu;q_0+2q), \tag{C1}$$

where we have employed the following definitions:

$$Q = \frac{p+\nu-q_0}{2}, \tag{C2a}$$

$$q_0 = q_0(p,t;\nu,-\mu), \tag{C2b}$$

$$q_0(p,t;\nu,\mu) = \begin{cases} |p-\nu| & \text{if } |p-\nu|\ge|t+\mu| \\ |p+\mu| & \text{if } |p-\nu|<|t+\mu| \text{ and} \\ & p+\nu+|t+\mu| \text{ is even} \\ |p+\mu|+1 & \text{if } |p-\nu|<|t+\mu| \text{ and} \\ & p+\nu+|t+\mu| \text{ is odd} \end{cases}, \tag{C2c}$$

$$\mathcal{G}(p,t;\nu,\mu;q) \equiv (-1)^{t+\mu}\int_\Omega Y_p^t(\theta,\phi)Y_\nu^\mu(\theta,\phi)Y_q^{-t-\mu}(\theta,\phi)\mathrm{d}\Omega \tag{C2d}$$

with $\mathrm{d}\Omega \equiv \sin(\theta)\mathrm{d}\theta\mathrm{d}\phi$, and Ω denoting 4π steradians. $\mathcal{G}$ is a Gaunt coefficient that is evaluated as follows:

$$\mathcal{G}(p,t;\nu,\mu;q) = (-1)^{t+\mu}\sqrt{\frac{(2p+1)(2\nu+1)(2q+1)}{4\pi}}$$
$$\times \begin{pmatrix} p & \nu & q \\ 0 & 0 & 0 \end{pmatrix}\begin{pmatrix} p & \nu & q \\ t & \mu & -t-\mu \end{pmatrix}, \tag{C2e}$$

where the two last factors are so-called Wigner 3-j symbols. $\hat{S}_{p,\nu}^{t,\mu}(\mathbf{b})$, introduced in the expansion in Eq. (16), can be expressed as follows [21]:

$$\hat{S}_{p,\nu}^{t,\mu}(\mathbf{b}) = 4\pi(-1)^{\nu+\mu+Q}\sum_{q=0}^Q (-1)^q \tilde{\psi}_{q_0+2q,t-\mu}^j(\mathbf{b})$$
$$\times \mathcal{G}(p,t;\nu,-\mu;q_0+2q). \tag{C3}$$

APPENDIX D: RADIAL INTEGRALS

We first consider the integral $I_l^{\mathbb{R}^3-\delta V_j}$, which is defined as

$$I_l^{\mathbb{R}^3-\delta V_j} \equiv \lim_{\delta R'\to 0}\left(\int_{\delta R'}^\infty h_l^{(1)}(k_{\mathrm{B}}r')j_l(k_jr')r'^2\mathrm{d}r'\right). \tag{D1}$$

Expanding the integrand for small arguments, we find

$$\lim_{r'\to 0}\left(h_l^{(1)}(k_{\mathrm{B}}r')j_l(k_jr')r'^2\right) = 0. \tag{D2}$$

This implies that the integrand is bounded in the limit $r'\to 0$, and consequently we may evaluate the limit before expressing the integral

$$I_l^{\mathbb{R}^3-\delta V_j} = \int_0^\infty h_l^{(1)}(k_{\mathrm{B}}r')j_l(k_jr')r'^2\mathrm{d}r'$$
$$= \frac{\pi}{2\sqrt{k_{\mathrm{B}}k_j}}\int_0^\infty H_{l+1/2}(k_{\mathrm{B}}r')J_{l+1/2}(k_jr')r'\mathrm{d}r'. \tag{D3}$$

The remaining integral has been expressed in [52]

$$I_l^{\mathbb{R}^3-\delta V_j} = -\frac{i}{k_{\mathrm{B}}}\frac{1}{k_j^2-k_{\mathrm{B}}^2}\left(\frac{k_j}{k_{\mathrm{B}}}\right)^l. \tag{D4}$$

Next, we express the finite part radial integral [40]

$$
\begin{aligned}
I_l^{V_j} &\equiv \int_0^{R_j} h_l^{(1)}(k_\mathrm{B} r') j_l(k_j r') r'^2 \mathrm{d}r' = \frac{M_l^j}{N_j^l N_j^{l,\mathrm{B}}} + \mathrm{i}\frac{\pi}{2}\sqrt{\frac{1}{k_j k_\mathrm{B}}}\frac{1}{k_j^2 - k_\mathrm{B}^2} \\
&\times \Big\{ [k_j R_j Y_{l+1/2}(k_\mathrm{B} R_j) J_{l+3/2}(k_j R_j) \\
&- k_\mathrm{B} R_j J_{l+1/2}(k_j R_j) Y_{l+3/2}(k_\mathrm{B} R_j)] - k_j^{l+1/2} k_\mathrm{B}^{-l-1/2}\frac{2}{\pi} \Big\}.
\end{aligned} \quad (D5)
$$

Finally, using the integrals expressed above, we have the radial integral needed to express the $B_{j,j}^{\alpha\alpha'}$ integrals,

$$
I_l^{\mathbb{R}^3 - V_j} \equiv \int_{R_j}^{\infty} h_l^{(1)}(k_\mathrm{B} r') j_l(k_j r') r'^2 \mathrm{d}r' = I_l^{\mathbb{R}^3 - \delta V_j} - I_l^{V_j}. \quad (D6)
$$

APPENDIX E: EXPANSION COEFFICIENTS OF $\mathbf{G_B(r,r')}$

To expand $\mathbf{G}_\mathrm{B}(\mathbf{r}, \mathbf{r}')$ on the background spherical wave functions, $\psi_{l,m}^{j,\mathrm{B}}(\mathbf{r}_j)$, cf. Eq. (5b), a slightly modified version of Eq. (19) for expressing the scalar Green's function, $g_\mathrm{B}(\mathbf{r}, \mathbf{r}')$, is applied:

$$
g_\mathrm{B}(\mathbf{r}, \mathbf{r}') = \mathrm{i}k_\mathrm{B}\sum_{\nu,\mu}(-1)^\mu \tilde{\psi}_{\nu,\mu}^{j,\mathrm{B}}(\mathbf{r}_j)\varphi_{\nu,-\mu}^\mathrm{B}(\mathbf{r}_j'). \quad (E1)
$$

We then express the elements of the background Green's tensor by the differential operators acting on $\varphi_{\nu,-\mu}^\mathrm{B}(\mathbf{r}_j')$:

$$
\begin{aligned}
\mathbf{G}_\mathrm{B}^{\alpha\alpha'}(\mathbf{r}, \mathbf{r}_d) &= \mathrm{i}k_\mathrm{B}\sum_{\nu,\mu}(-1)^\mu \psi_{\nu,\mu}^{j,\mathrm{B}}(\mathbf{r}_j)/(N_\nu^{j,\mathrm{B}}) \\
&\times \Big(\delta_{\alpha\alpha'}\varphi_{\nu,-\mu}^\mathrm{B}(\mathbf{r}_j') + \frac{1}{k_\mathrm{B}^2}\sum_{\gamma_{\alpha,\alpha'}} g_{\gamma_{\alpha,\alpha'}}\varphi_{\nu(\gamma_{\alpha,\alpha'}),\mu^*(\gamma_{\alpha,\alpha'})}^\mathrm{B}(\mathbf{r}_j') \Big),
\end{aligned} \quad (E2)
$$

where $\mu^*(\gamma_{\alpha,\alpha'}) \equiv -\mu + \gamma_{\alpha,\alpha'}''$. This relation is what we wanted: an expansion of the elements of the background Green's tensor on $\psi_{\nu,\mu}^{j,\mathrm{B}}(\mathbf{r}_j)$. The expansion coefficients are thus as given in Eq. (24).

ACKNOWLEDGMENTS

REFERENCES

1. V. P. Bykov, "Spontaneous emission from a medium with a band spectrum," Sov. J. Quantum Electron. **4**, 861–871 (1975).
2. E. Yablonovitch, "Inhibited spontaneous emission in solid-state physics and electronics," Phys. Rev. Lett. **58**, 2059–2062 (1987).
3. S. John, "Strong localization of photons in certain disordered dielectric superlattices," Phys. Rev. Lett. **58**, 2486–2489 (1987).
4. K. R. Catchpole and A. Polman, "Plasmonic solar cells," Opt. Express **16**, 21793–21800 (2008).
5. N. Liu, M. Hentschel, T. Weiss, A. P. Alivisatos, and H. Giessen, "Three-dimensional plasmon rulers," Science **332**, 1407–1410 (2011).
6. J. Z. Zhang and C. Noguez, "Plasmonic optical properties and applications of metal nanostructures," Plasmonics **3**, 127–150 (2008).
7. M. Dems, I.-S. Chung, P. Nyakas, S. Bischoff, and K. Panajotov, "Numerical methods for modeling photonic-crystal VCSELs," Opt. Express **18**, 16042–16054 (2010).
8. A. Taflove and S. Hagness, *Computational Electrodynamics: The Finite-Difference Time-Domain Method*, 3rd ed. (Artech House, 2005).
9. J. Reddy, *An Introduction to the Finite Element Method*, 3rd ed. (McGraw-Hill Science/Engineering/Math, 2005).
10. K. Busch, M. König, and J. Niegemann, "Discontinuous Galerkin methods in nanophotonics," Laser Photon. Rev. **5**, 773–809 (2011).
11. M. G. Moharam, E. B. Grann, D. A. Pommet, and T. K. Gaylord, "Formulation for stable and efficient implementation of the rigorous coupled-wave analysis of binary gratings," J. Opt. Soc. Am. A **12**, 1068–1076 (1995).
12. L. C. Botten, R. C. McPhedran, N. A. Nicorovici, A. A. Asatryan, C. M. de Sterke, P. A. Robinson, K. Busch, G. H. Smith, and T. N. Langtry, "Rayleigh multipole methods for photonic crystal calculations," Prog. Electromagn. Res. **41**, 21–60 (2003).
13. J. Berenger, "A perfectly matched layer for the absorption of electromagnetic waves," J. Comput. Phys **114**, 185–200 (1994).
14. L. Novotny and B. Hecht, *Principles of Nano-Optics*, 1st ed. (Cambridge University, 2006).
15. A. F. Peterson, S. L. Ray, and R. Mittra, *Computational Methods for Electromagnetics*, 1st ed. (IEEE, 1998).
16. B. T. Draine and P. J. Flatau, "Discrete-dipole approximation for scattering calculations," J. Opt. Soc. Am. A **11**, 1491–1499 (1994).
17. H. Levine and J. Schwinger, "On the theory of diffraction by an aperture in an infinite plane screen. I," Phys. Rev. **74**, 958–974 (1948).
18. J. D. Jackson, *Classical Electrodynamics*, 3rd ed. (Wiley, 1998).
19. C.-T. Tai, *Dyadic Green Functions in Electromagnetic Theory*, 2nd ed. (IEEE, 1994).
20. M. Paulus, P. Gay-Balmaz, and O. J. F. Martin, "Accurate and efficient computation of the Green's tensor for stratified media," Phys. Rev. E **62**, 5797–5807 (2000).
21. P. A. Martin, *Multiple Scattering. Interaction of Time-Harmonic Waves with N Obstacles*, 1st ed. (Cambridge University, 2006).
22. P. T. Kristensen, P. Lodahl, and J. Mørk, "Light propagation in finite-sized photonic crystals: multiple scattering using an electric field integral equation," J. Opt. Soc. Am. B **27**, 228–237 (2010).
23. G. Mie, "Articles on the optical characteristics of turbid tubes, especially colloidal metal solutions," Ann. Phys. **25**, 377–445 (1908).
24. Y. L. Xu, "Electromagnetic scattering by an aggregate of spheres," Appl. Opt. **34**, 4573–4588 (1995).
25. D. W. Mackowski and M. I. Mishchenko, "Calculation of the T matrix and the scattering matrix for ensembles of spheres," J. Opt. Soc. Am. A **13**, 2266–2278 (1996).
26. F. J. García de Abajo, "Multiple scattering of radiation in clusters of dielectrics," Phys. Rev. B **60**, 6086–6102 (1999).
27. M. Born and E. Wolf, *Principles of Optics: Electromagnetic Theory of Propagation Interference and Diffraction of Light*, 6th ed. (Pergamon, 1981).
28. O. J. F. Martin and N. B. Piller, "Electromagnetic scattering in polarizable backgrounds," Phys. Rev. E **58**, 3909–3915 (1998).
29. R. Sprik, B. A. van Tiggelen, and A. Lagendijk, "Optical emission in periodic dielectrics," Europhys. Lett. **35**, 265–270 (1996).
30. E. M. Purcell, "Proceedings of the American Physical Society, b10. Spontaneous emission probabilities at radio frequencies," Phys. Rev. **69**, 674 (1946).
31. K. M. Lee, P. T. Leung, and K. M. Pang, "Dyadic formulation of morphology-dependent resonances. I. Completeness relation," J. Opt. Soc. Am. B **16**, 1409–1417 (1999).
32. P. T. Kristensen, C. V. Vlack, and S. Hughes, "Generalized effective mode volume for leaky optical cavities," Opt. Lett. **37**, 1649–1651 (2012).
33. J. R. de Lasson, P. T. Kristensen, and J. Mørk, "Multiple-scattering formalism beyond the quasistatic approximation: analyzing resonances in plasmonic chains," AIP Conf. Proc. **1475**, 158–160 (2012).
34. A. D. Yaghjian, "Electric dyadic Green's functions in the source region," Proc. IEEE **68**, 248–263 (1980).

35. F. Capolino, *Theory and Phenomena of Metamaterials*, 1st ed. (CRC Press, 2009).

36. R. A. Shore and A. D. Yaghjian, "Traveling waves on two- and three-dimensional periodic arrays of lossless scatterers," Radio Sci. **42**, RS6S21 (2007).

37. P. A. Martin, "Multiple scattering and the Rehr–Albers–Fritzsche formula for the propagator matrix," J. Phys. A **31**, 8923 (1998).

38. V. N. Pustovit and T. V. Shahbazyan, "Plasmon-mediated superradiance near metal nanostructures," Phys. Rev. B **82**, 075429 (2010).

39. E. S. C. Ching, P. T. Leung, A. Maassen van den Brink, W. M. Suen, S. S. Tong, and K. Young, "Quasinormal-mode expansion for waves in open systems," Rev. Mod. Phys. **70**, 1545–1554 (1998).

40. M. R. Spiegel, S. Lipschutz, and J. Liu, *Schaum's Outline of Mathematical Handbook of Formulas and Tables*, 3rd ed. (McGraw-Hill, 2008).

41. S. A. Maier, *Plasmonics: Fundamentals and Applications*, 1st ed. (Springer, 2007).

42. V. Myroshnychenko, J. Rodriguez-Fernandez, I. Pastoriza-Santos, A. M. Funston, C. Novo, P. Mulvaney, L. M. Liz-Marzan, and F. J. García de Abajo, "Modelling the optical response of gold nanoparticles," Chem. Soc. Rev. **37**, 1792–1805 (2008).

43. E. Hao and G. C. Schatz, "Electromagnetic fields around silver nanoparticles and dimers," J. Chem. Phys. **120**, 357–366 (2004).

44. M. Chen, Y.-F. Chau, and D. Tsai, "Three-dimensional analysis of scattering field interactions and surface plasmon resonance in coupled silver nanospheres," Plasmonics **3**, 157–164 (2008).

45. P. K. Jain, W. Huang, and M. A. El-Sayed, "On the universal scaling behavior of the distance decay of plasmon coupling in metal nanoparticle pairs: a plasmon ruler equation," Nano Lett. **7**, 2080–2088 (2007).

46. N. Harris, M. D. Arnold, M. G. Blaber, and M. J. Ford, "Plasmonic resonances of closely coupled gold nanosphere chains," J. Phys. Chem. C **113**, 2784–2791 (2009).

47. A. F. Koenderink, "On the use of Purcell factors for plasmon antennas," Opt. Lett. **35**, 4208–4210 (2010).

48. Y. Chen, T. R. Nielsen, N. Gregersen, P. Lodahl, and J. Mørk, "Finite-element modeling of spontaneous emission of a quantum emitter at nanoscale proximity to plasmonic waveguides," Phys. Rev. B **81**, 125431 (2010).

49. S. Raza, G. Toscano, A.-P. Jauho, M. Wubs, and N. A. Mortensen, "Unusual resonances in nanoplasmonic structures due to nonlocal response," Phys. Rev. B **84**, 121412 (2011).

50. M. Liu, T.-W. Lee, S. K. Gray, P. Guyot-Sionnest, and M. Pelton, "Excitation of dark plasmons in metal nanoparticles by a localized emitter," Phys. Rev. Lett. **102**, 107401 (2009).

51. F. J. García de Abajo, "Relativistic energy loss and induced photon emission in the interaction of a dielectric sphere with an external electron beam," Phys. Rev. B **59**, 3095–3107 (1999).

52. J. Kellendonk and S. Richard, "Weber–Schafheitlin-type integrals with exponent 1," Integral Transforms Spec. Funct. **20**, 147–153 (2009).